PHYSICAL REVIEW E **100**, 052605 (2019)

From normal diffusion to superdiffusion: Photothermal heating of plasmonic core-shell microgels

Nico Carl[*]
Physical Chemistry, University of Paderborn, 33098 Paderborn, Germany

Julian Sindram
Institut für Physikalische Chemie I: Kolloide und Nanooptik, Heinrich-Heine-Universität Düsseldorf, 40225 Düsseldorf, Germany

Markus Gallei
Chair in Polymer Chemistry, Saarland University, Campus Saarbrücken C4 2, 66123 Saarbrücken, Germany

Stefan U. Egelhaaf
Condensed Matter Physics Laboratory, Heinrich-Heine-University Düsseldorf, 40225 Düsseldorf, Germany

Matthias Karg[†]
Institut für Physikalische Chemie I: Kolloide und Nanooptik, Heinrich-Heine-Universität Düsseldorf, 40225 Düsseldorf, Germany

(Received 11 July 2019; published 12 November 2019)

The motion of core-shell colloids during laser heating is studied using angle-dependent pump-probe dynamic light scattering. The cores consist of a single spherical gold nanoparticle whose localized surface plasmon resonance has a strong spectral overlap with the wavelength of the pump laser. They are homogeneously encapsulated in thick hydrogel shells composed of either chemically cross-linked poly-*N*-isopropylacrylamide or poly[2-(2-methoxyethoxy)ethyl methacrylate], both of which exhibit a temperature-dependent volume phase transition. Thus, upon heating beyond the transition temperature, the hydrogel shells shrink. Intensity-time autocorrelation functions are recorded while illuminating the samples with the pump laser and hence heating the gold cores. With increasing laser intensity, the dynamics changes from normal Brownian motion to superdiffusion. Nevertheless, in the high-q limit, the relaxation times can be extracted and used to estimate the temperature increase, which can reach almost 10 K. This causes a significant deswelling of the hydrogel shells, which is also measured.

DOI: 10.1103/PhysRevE.100.052605

I. INTRODUCTION

Noble-metal nanoparticles can absorb electromagnetic energy efficiently due to the excitation of localized surface plasmons (LSPs) [1,2]. These plasmons result from collective oscillations of the electron gas in resonance with the incident electromagnetic wave. Small nanoparticles (NPs) of spherical shape, which are below 100 nm in diameter for gold, show single resonances that correspond to dipole excitations [3]. The frequency at which such resonances occur in dilute noninteracting systems depends on the NP size and the refractive index of the surrounding environment [4–6]. The energy absorbed by such particles is typically dissipated nonradiatively [7].

The most frequent way of energy dissipation is the transformation into heat [8]. This results in a temperature increase in the surroundings of the NPs. The steady-state temperature profile in the vicinity of an absorbing particle with an absorption cross section σ_{abs} under continuous illumination is given by [9,10]

$$\Delta T = \begin{cases} \frac{\sigma_{\mathrm{abs}} I}{4\pi\kappa_s R}, & r \leqslant R \\ \frac{\sigma_{\mathrm{abs}} I}{4\pi\kappa_s R}\frac{R}{r}, & r > R. \end{cases} \tag{1}$$

Here I is the incident irradiance (up to 1.2×10^4 W cm^{-2} for our setup), κ_s the thermal conductivity of the surrounding medium ($\kappa_s = 0.591$ W m^{-1} K^{-1} for water at 25 °C), R the particle radius (e.g., 7.5 nm for our smallest gold NPs), and r the distance from the particle center. Thus, at high enough irradiance, a significant heating of the particle environment can be achieved, even for relatively small nanoparticles [see temperature profiles in Figs. 1(d) and 1(e)]. Compared to molecular absorbers such as organic dyes, σ_{abs} is larger, by several orders of magnitude, for plasmonic NPs (approximately equal to 1.6×10^{-16} m^2 for a 15-nm-diam gold NP). At the same time plasmonic NPs do not suffer from photobleaching and photoblinking, allowing for much longer observation times and continuous illumination for heating. The heat generated in the vicinity of the NPs induces changes in the viscosity $\eta(T)$ and refractive index $n(T)$ of the surrounding medium as both are temperature dependent. The changes in n are the basis for the photothermal detection of plasmonic NPs

---

[*] Also at Institut Laue–Langevin, 38042 Grenoble Cedex 9, France.

[†] karg@hhu.de, http://www.karg.hhu.de

2470-0045/2019/100(5)/052605(12)

[8,11–13]. Furthermore, plasmonic NPs are interesting as local heat sources that allow one to fabricate anisotropic surface patterns [14] or nano-oscillators [15] by simple light irradiation when combined with a temperature-sensitive matrix containing, for example, azobenzene dyes [14] or thermoresponsive polymers [16]. A prominent example for thermoresponsive polymers is poly-*N*-isopropylacrylamide (PNIPAM) that shows a lower critical solution temperature (LCST) in water at a temperature of approximately 32 °C [17]. Below the LCST PNIPAM is in a coil state, while a transition to a less hydrated globule state is observed when the LCST is passed [18]. Due to this behavior, PNIPAM based microgels, i.e., submicrometer-size objects with an internal gel-like structure of cross-linked PNIPAM polymer, show a pronounced volume phase transition in water [19]. In contrast to their macroscopic counterparts (macrogels), microgels undergo significantly faster shrinking and swelling in water due to their much larger surface-to-volume ratio. This makes thermoresponsive microgels very interesting for applications in sensing and actuation including photothermal heating. Different ways of combining microgels with plasmonic metal nanoparticles are known from the literature as summarized in related review articles [20,21]. Das *et al.* used thermoresponsive microgels that were loaded with gold nanorods and studied the effect of laser heating on the swelling state of the microgels [22]. Using fixed angle dynamic light scattering (DLS), the authors determined the hydrodynamic microgel size in the on or off state of the heating laser. They found reversible swelling and deswelling with a pronounced change in microgel volume for many cycles. Similarly, Lehmann *et al.* used DLS to study the laser-induced shrinking of PNIPAM microgels that were infiltrated with spherical gold NPs [23]. Hormeño *et al.* used optical tweezers to study the photothermally induced shrinkage of trapped PNIPAM microgels that were loaded with gold NPs [24]. The same authors also studied optically trapped core-shell microgels with single gold NP cores [25]. The change in optical extinction in response to photothermal heating was studied by Rodríguez-Fernández *et al.* using core-shell microgels with single gold nanorods as cores [26]. Similarly, Murphy *et al.* used laser flash photolysis to investigate the extinction of core-shell microgels with gold NP cores upon laser-induced shrinkage and the relaxation kinetics during reswelling [27]. While these works show that photothermal heating of gold nanoparticles can be used to trigger the volume phase transition of thermoresponsive microgels, little is known about the effect on particle motion. However, several authors have shown that photothermal heating affects the Brownian motion of metal NPs considerably [28–30]. Thus one could expect that also the motion of hybrid microgels with encapsulated metal NPs will significantly change in response to laser heating.

In this work we systematically address the effect of laser heating on the diffusion of absorbing plasmonic colloids using a pump-probe (PP) dynamic light scattering setup. Our aims are (i) to identify whether continuous illumination of the colloids with a pump laser causes a change in temperature and in turn also the viscosity in the scattering volume that ultimately will affect the diffusion and (ii) to investigate whether laser heating induces a collapse of thermoresponsive hydrogel shells that surround absorbing plasmonic particles, i.e., for core-shell microgels. To do so, we first perform reference measurements to study the relevance of the photon pressure from the pump laser using nonabsorbing polystyrene particles. Subsequently, gold nanoparticles without hydrogel shells are investigated as a plasmonic reference system. Next we study the influence of photothermal heating on core-shell particles consisting of spherical gold nanoparticle cores and hydrogel shells composed of either chemically cross-linked PNIPAM or poly[2-(2-methoxyethoxy)ethyl methacrylate].

II. THEORETICAL BACKGROUND

Angle-dependent DLS allows for the study of the diffusion of colloids. In a DLS measurement the intensity-time autocorrelation function (ICF) $g_2(\boldsymbol{q},\tau)$ is calculated from the scattering intensity $I(\boldsymbol{q},t)$ measured at the scattering vector $\boldsymbol{q}$ and time t with the delay time τ:

$$g_2(\boldsymbol{q},\tau)=\frac{\langle I(\boldsymbol{q},t)I(\boldsymbol{q},t+\tau)\rangle}{\langle I(\boldsymbol{q},t)\rangle^2}. \tag{2}$$

Here $g_2(\boldsymbol{q},\tau)$ can be used to calculate the intermediate scattering function $f(q,\tau)$ [31]:

$$f(q,\tau)=\sqrt{g_2(q,\tau)-1}. \tag{3}$$

For dilute dispersions of monodisperse scattering objects $f(q,\tau)$ follows an exponential decay providing the diffusion coefficient D_0:

$$f(q,\tau)=\exp(-q^2D_0\tau)=\exp\left(-\frac{\tau}{\tau_r}\right). \tag{4}$$

Here τ_r is the relaxation time and q is the magnitude of the scattering vector $\boldsymbol{q}$ that can be calculated based on the refractive index of the dispersing medium n and the laser wavelength λ:

$$|\boldsymbol{q}|=q=\frac{4\pi n}{\lambda}\sin\left(\frac{\theta}{2}\right). \tag{5}$$

Strictly, n varies with temperature. However, the variation within a relatively small temperature window is small (approximately equal to 0.2% comparing $T=298.15$ and 318.15 K) and hence the temperature dependence of n is neglected in our DLS experiments under photothermal heating conditions. In the unperturbed case and in dilute dispersion colloids undergo Brownian motion with a diffusion coefficient D_0 that is described by the Stokes-Einstein equation

$$D_0=\frac{k_BT}{6\pi\eta R_h}. \tag{6}$$

Here k_B is the Boltzmann constant, T the temperature, η the viscosity of the dispersion medium, and R_h the hydrodynamic radius of the diffusing particles. Thus, for the calculation of R_h, knowledge of the temperature in the vicinity of the particle is crucial. A photothermal heating event might lead to an increase in the effective temperature in the scattering volume. At the same time the temperature dependence of the viscosity of the dispersing medium has to be considered. For water the temperature dependence of the viscosity can be approximated by a polynomial function [32]

$$\eta(T)=A[\Delta T+a\Delta T^2+b\Delta T^3+c\Delta T^4]^{-\gamma}. \tag{7}$$

For water $A = 802.3\ \mathrm{cP\,K}^{\gamma}$, $a = 3.474 \times 10^{-3}\ \mathrm{K}^{-1}$, $b = -1.741 \times 10^{-5}\ \mathrm{K}^{-2}$, $c = 2.772 \times 10^{-8}\ \mathrm{K}^{-3}$, $\gamma = 1.530$, and $\Delta T = T - 225.3$ K [32].

III. EXPERIMENT

A. Colloid synthesis

Two classes of absorbing colloids were synthesized: citrate-stabilized and hydrogel encapsulated spherical gold colloids. Citrate-stabilized gold nanoparticles of two different sizes were synthesized using a standard reduction protocol [33]. These samples will be labeled by Au_x throughout this work, with x indicating the average nanoparticle diameter as determined by TEM. Core-shell colloids with gold cores and hydrogel shells were prepared by seeded precipitation polymerization [34]. This two-step approach employs citrate-stabilized gold nanoparticles prepared by the protocol of Turkevich *et al.* [35] that are subsequently surface functionalized with butenylamine and then used as seeds in the precipitation polymerization. We synthesized core-shell colloids with two different chemically cross-linked hydrogel shells consisting of either PNIPAM or poly[2-(2-methoxyethoxy)ethyl methacrylate] ($\mathrm{PMEO_2MA}$). The gold cores of these core-shell particles were subsequently increased in size using seeded growth [36]. All core-shell microgels will be labeled as Au_x-PNIPAM or Au_x-$\mathrm{PMEO_2MA}$ in this work, depending on the shell material, with x indicating the average diameter of the gold nanoparticle cores as determined by TEM. We also prepared gold-free hydrogel colloids, as nonabsorbing but temperature-sensitive reference particles, by chemical dissolution of the gold cores of the core-shell particles. These purely organic microgels are labeled PNIPAM. Detailed information on the synthesis of all particles can be found in the Appendix. Figure 1(a) provides a schematic overview of the different colloids that we used for pump-probe DLS experiments. Figures 1(b) and 1(c) present the results of UV-vis absorbance measurements of the different colloids. The citrate-stabilized gold nanoparticles of both sizes show single peaks in absorbance due to their dipolar LSP resonances [Fig. 1(b)]. Due to a smaller restoring force, the resonance of the larger particles appears at slightly longer wavelengths and is more intense as compared to the smaller particles [33]. Despite the difference in intensity, the LSP resonance maxima of both particle sizes are close to the wavelength of the pump laser ($\lambda_{\mathrm{Nd:YAG}} = 532$ nm), as indicated by the vertical dashed line. In contrast, the absorbance for both particle batches is negligible at the center wavelength of the probe laser ($\lambda_{\mathrm{HeNe}} = 632.8$ nm). The spectra of the Au_{35}-PNIPAM core-shell microgels [Fig. 1(c)] reveal LSP resonance peaks attributed to the gold nanoparticle cores, again with spectral positions very close to the wavelength of the pump laser. In contrast, the spectra recorded for the empty hydrogel particles (PNIPAM, spectra in gray) do not feature resonance peaks supporting the success of the core dissolution. Instead these spectra show a continuous increase of the absorbance for decreasing wavelength. This increase in absorbance is related to scattering from the relatively large hydrogel shell. Both samples analyzed in Fig. 1(c) show also a temperature-dependent behavior. In particular in the short-wavelength region, where the scattering contribution is the strongest, the absorbance increases with increasing temperature. This increase is related to an increase in scattering that is caused by an increase of the effective refractive index of the shrinking hydrogel shells [34]. Figures 1(d) and 1(e) show the theoretical single-particle temperature profiles in the vicinity of the small and large gold particles for different nominal laser powers ($\lambda = 532$ nm) calculated using Eq. (1). With increasing laser power, the temperature inside and outside the particles increases. The larger particles show a relative temperature increase that is roughly one order of magnitude higher than for the small particles. More details on the calculation of these temperature profiles can be found in the Appendix.

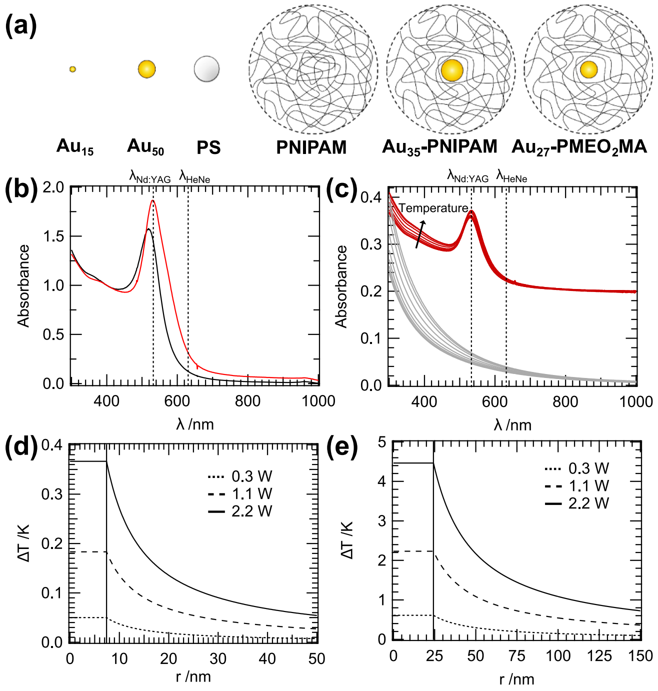

FIG. 1. (a) Schematic illustration of the different colloids used in this study. (b) UV-vis absorbance spectra of Au_{15} (black) and Au_{50} (red) normalized at $\lambda = 400$ nm. (c) UV-vis absorbance spectra of PNIPAM (gray) and Au_{35}-PNIPAM (red) at temperatures ranging from 10° to 50°. The data for Au_{35}-PNIPAM are shifted horizontally (fixed offsets) for clearer representation. The calculated temperature profiles are shown for (d) Au_{15} and (e) Au_{50} at three different nominal laser powers according to Eq. (1).

Table I summarizes important sample parameters for all samples relevant to this study, including commercial polystyrene (PS) particles that were used as a nonabsorbing and temperature-insensitive reference sample. Details for the calculations of the absorption cross sections σ_{abs} as well as images of the different colloids recorded by TEM can be found in the Appendix.

B. Pump-probe DLS

A schematic representation of the light scattering setup used for our PP DLS experiments is shown in Fig. 2. The sample is placed in the center of a classical goniometer setup that allows positioning of the detection optics in a wide angular range. A probe laser (HeNe) with a wavelength $\lambda = 632.8$ nm and a pump laser (Nd:YAG) with a wavelength

TABLE I. Position of the LSP resonance λ_{LSP} from UV-vis absorbance spectroscopy, theoretical absorption cross section σ_{abs} at 532 nm, gold nanoparticle or core radii $R_{\mathrm{Au\text{-}NP}}$ from analysis of TEM and SEM images, and hydrodynamic radii R_h from DLS.

Sample	λ_{LSPR} (nm)	σ_{abs} (nm^2)	$R_{\mathrm{Au\text{-}NP}}$ (nm)	R_h (nm)
Au_{15}	518	1.6×10^2	7.4 ± 1.5[a]	9.2 ± 0.1[b]
Au_{50}	532	6.4×10^3	24 ± 4[a]	27.0 ± 0.1[b]
PS				35.0 ± 0.1[b]
PNIPAM				120 ± 0.4[b]
Au_{35}-PNIPAM	529		18 ± 1[a]	115 ± 1.5[b]
Au_{27}-$\mathrm{PMEO_2MA}$	537		13.7 ± 2.0[a]	127.2 ± 0.3[b]

[a] Standard deviation of a Gaussian size distribution.

[b] Statistical error.

$\lambda = 532$ nm are aligned on the same beam path using a dichroic mirror. Both lasers are then focused on the sample center with a biconvex lens with a focal length of 350 mm. Reference measurements using static light scattering (SLS) on PS reference particles shown in the Appendix [Fig. 9(a)] confirm the good alignment of the two beams. In order to block off scattered light from the pump laser, a longpass filter with a cutoff wavelength $\lambda = 600$ nm is placed in front of the detection optics. The transmission spectrum of the filter and reference measurements that show that scattered light from the pump laser is efficiently blocked are provided in the Appendix [Figs. 9(c)–9(f)]. We performed pump-probe experiments with all colloids listed in Table I using the HeNe laser as a probe laser to record ICFs. The nominal power of the pump laser was adjusted between 0 and 2.2 W corresponding to irradiances up to $1.2 \times 10^4\ \mathrm{W\,cm^{-2}}$. Details on the calculation of the irradiance and the determination of the laser power are presented in the Appendix.

IV. RESULTS AND DISCUSSION

A. Effect of laser heating on diffusion of gold nanoparticles

Angle-dependent PP DLS experiments were performed at various pump powers using the Au_{15} and Au_{50} particles in dilute aqueous dispersion. Figure 3(a) shows representative ICFs of both samples recorded at 0 and 2.2 W.

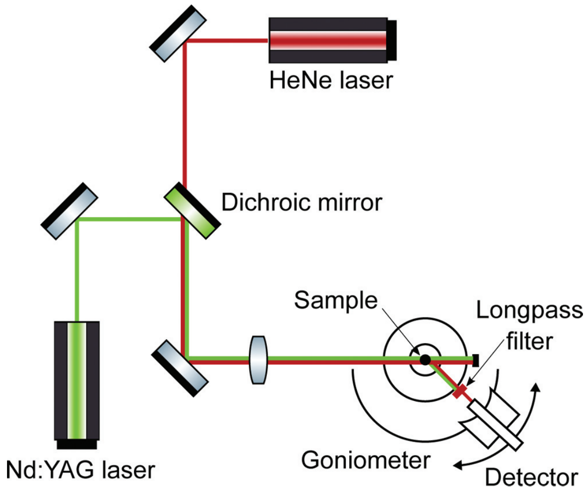

FIG. 2. Schematic representation of the PP DLS setup.

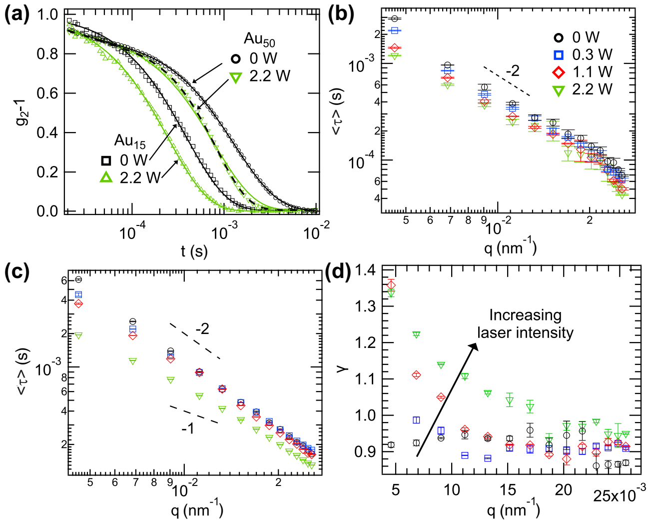

FIG. 3. (a) ICFs of Au_{15} and Au_{50} at laser powers of 0 and 2.2 W at a scattering angle of 30°. The solid lines represent fits to Eq. (8) and the dashed lines fits to Eq. (9). The average relaxation time $\langle\tau\rangle$ is shown as a function of q for (b) Au_{15} and (c) Au_{50} at laser powers of 0, 0.3, 1.1, and 2.2 W. (d) Dependence of the compressing exponent γ on q for Au_{50} at laser powers of 0.3, 1.1, and 2.2 W. The symbols are the same as indicated in (b).

For both samples, the ICFs recorded at 0 W (black symbols) show a decay behavior that is typical for normal Brownian motion of colloids with low polydispersity. These ICFs could be analyzed by the method of cumulants according to the procedure described by Frisken [37]:

$$g_2(\boldsymbol{q},\tau) = \beta \exp\left(-2\frac{\tau}{\tau_r}\right)\left(1+\frac{\mu_2}{2}\tau^2\right)^2 + B. \qquad (8)$$

Here β is the intercept of the ICF that is typically a measure for the signal-to-noise ratio of the setup, τ_r the relaxation time, μ_2 the second cumulant, and B a baseline correction for the ICF. The cumulant fits (solid lines) nicely match the experimentally measured data of both samples at 0 W. For 2.2 W, the ICFs of both samples (green symbols) decay significantly faster than at 0 W. The data recorded for the Au_{15} particles could still be described sufficiently well by the cumulant fit (solid line) providing $\tau_r = 0.49$ ms, which is significantly smaller than the obtained relaxation time for 0 W pump power (0.78 ms). This strong decrease in relaxation time indicates an increase of the diffusion coefficient related to a significant increase of the average effective temperature in the scattering volume due to photothermal heating. In contrast, the cumulant fit (green solid line) fails to match the data recorded for the Au_{50} particles at 2.2 W. Instead, here the data can be described by a compressed exponential function (black dashed line) [38]

$$g_2(\boldsymbol{q},\tau) - 1 = \beta \exp\left[-2\left(\frac{\tau}{\tau_r}\right)^{\gamma}\right] + B. \qquad (9)$$

Here β is a scaling prefactor, γ the compressing ($\gamma > 1$) or stretching ($\gamma < 1$) exponent, and B a baseline correction.

We want to highlight that Eq. (9) also describes the ICFs very well where the cumulant fit can still be applied successfully, for example, in the case of 0 W pump power. For the sake of clarity, we do not include these fits in Fig. 3(a). In the following all ICFs recorded for both samples at various pump powers and scattering angles are analyzed by Eq. (9), providing the respective relaxation time τ_r as well as the compressing exponent γ. Measurements are performed in a wide angular range, thus covering a broad range of q in order to investigate the diffusion of the particles. To account for the effect of the exponent γ, average relaxation times $\langle\tau\rangle$ are calculated from τ_r according to [39]

$$\langle\tau\rangle = \frac{\tau_r}{\gamma}\Gamma\left(\frac{1}{\gamma}\right). \tag{10}$$

Here Γ denotes the Gamma function $\Gamma(n) = (n-1)!$. Figure 3(b) shows the q dependence of $\langle\tau\rangle$ obtained from measurements of the Au_{15} particles analyzed by Eqs. (9) and (10). For each pump power $\langle\tau\rangle$ scales with q^{-2}, indicating that normal diffusion is observed. At the same time the compressing exponents γ are close to unity for all measurements on this sample, independent of the pump power, as expected for normal diffusion of monodisperse colloids. However, a decrease in $\langle\tau\rangle$ with increasing pump power is observed over the whole q range. This decrease corresponds to an increasing diffusion coefficient that can be attributed to an increase of the effective temperature accompanied by a decrease in viscosity in the scattering volume due to photothermal heating with the pump laser. Figure 3(c) shows the resulting q dependence of $\langle\tau\rangle$ for the Au_{50} particles. At higher pump powers a significant deviation from normal diffusion is observed with a scaling that approaches q^{-1}. Here the detected motion shows a transition from normal diffusion to superdiffusion. Figure 3(d) shows the compression exponent γ as a function of q for different pump powers. In the high-q limit γ asymptotically approaches unity for all pump powers. At lower q, γ increases significantly with increasing pump power.

We propose that the local temperature increase around the particles leads to an effective temperature increase within the scattering volume. Consequently, a convection roll is formed as proposed earlier by Schaertl and Roos [28]. This results in a superposition of the Brownian motion of the particles with a flow due to the convection roll. For such a type of motion $\langle\tau\rangle$ scales with $q^{-\alpha}$, with $\alpha < 2$, as also found for blends of conjugated polymers and fullerenes [40]. Such a superposition of motion is often accompanied by the observation of compressed exponential correlation functions [38], which explains our observation for the Au_{50} particles. We attribute the q dependence of the compressing exponent γ to the following: At low q, phenomena occur on relatively large length scales, whereas at high q rather small scales are probed. Caused by the photothermal heating, convection rolls form with length scales that are smaller than the size of the overall scattering volume but larger than the particle diameter. In the high-q limit γ approaches unity independent of the pump power and thus normal diffusion is observed. In the lower-q region the flow induced by the temperature increase becomes significant and γ deviates from unity with increasing values for increasing pump power at a fixed q. Thus the values γ for a fixed q in the lower-q range can be taken as a measure of the flow caused by the convection rolls. Furthermore, due to the different time dependences, in general, superdiffusion dominates diffusive motion on large timescales corresponding to large length scales, i.e., small values of q.

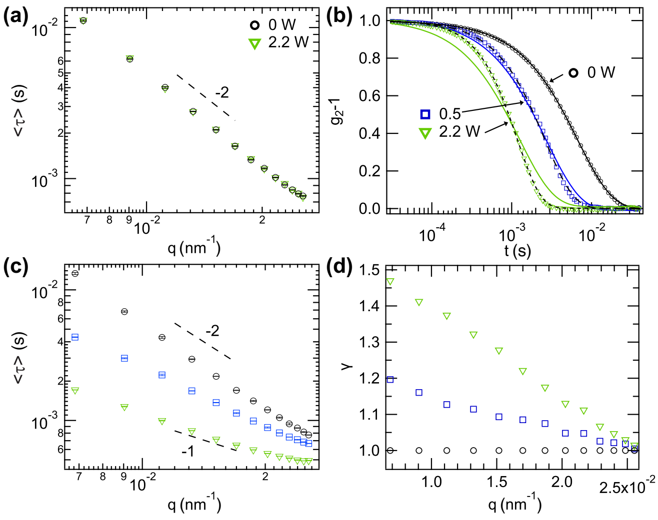

FIG. 4. (a) The q dependence of $\langle\tau\rangle$ for a nonabsorbing PNIPAM microgel at laser powers of 0 and 2.2 W. (b) ICF of Au_{35}-PNIPAM core-shell microgels at laser powers of 0, 0.5, and 2.2 W. The solid lines represent fits to Eq. (8) and the dashed lines fits to Eq. (9). (c) The q dependence of $\langle\tau\rangle$ and (d) compressing exponent γ for Au_{35}-PNIPAM core-shell microgels at laser powers of 0, 0.5, and 2.2 W. The symbols are the same as indicated in (b). The error bars are on the order of the symbol size and are excluded for clearer representation in (d).

B. Effect of photothermal heating on diffusion of core-shell microgels

Knowing that our pump laser is suitable to provide efficient photothermal heating of near-resonant absorbing gold NPs, we will now investigate thermoresponsive microgels by PP DLS. Before discussing the results from core-shell microgels with absorbing gold cores, we will first address purely organic PNIPAM microgels that are prepared by dissolution of the gold cores. Details on the dissolution of the cores can be found in the Appendix. Since these PNIPAM microgels show a pronounced volume phase transition behavior with a continuous decrease in hydrodynamic size between 10 °C and 50 °C, we expect to observe a clear change of the diffusion coefficient when the local temperature in the scattering volume is changed.

Figure 4(a) shows $\langle\tau\rangle$ as a function of q for the PNIPAM microgels measured at laser powers of 0 and 2.2 W. In this double-logarithmic representation both data sets show a linear decrease of $\langle\tau\rangle$ with q and slopes of -2, as expected for normal diffusion. Furthermore, the data for the two pump powers nicely overlap. The diffusion of the nonabsorbing PNIPAM microgels is not affected by the pump laser. Consequently, we conclude that the pump laser does not lead to a significant change of temperature in the scattering volume.

Pump-probe experiments with the core-shell microgels containing absorbing gold cores reveal a different behavior.

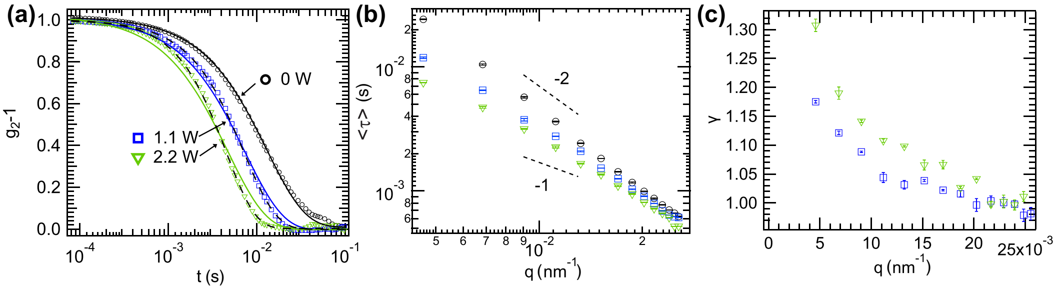

FIG. 5. (a) ICFs of Au$_{27}$-PMEO$_2$MA at laser intensities of 0, 1.1, and 2.2 W. The solid lines represent fits to Eq. (8) and the dashed lines fits to Eq. (9). (b) The q dependence of $\langle\tau\rangle$ is shown for Au$_{27}$-PMEO$_2$MA at laser intensities of 0, 1.1, and 2.2 W. The symbols are the same as indicated as in (a). (c) Dependence of the compressing exponent γ on q for laser intensities of 0, 1.1, and 2.2 W of Au$_{27}$-PMEO$_2$MA. The symbols are the same as indicated in (a).

Figure 4(b) shows the ICFs recorded from the Au$_{35}$-PNIPAM microgels at different laser powers. We observe results similar to those for the Au$_{50}$ particles: At 0 W, the ICF shows a typical decay that can be well described by the cumulant fit (solid line). With increasing pump power, the ICFs decay faster and the cumulant fit fails to describe the data (solid lines). The ICFs become more compressed with increasing pump power and can be well described by Eq. (9) with compressing exponents $\gamma > 1.0$ (dashed lines). The $\langle\tau\rangle$ determined from analysis with Eqs. (9) and (10) decrease from 14 ms (0 W) to 4 ms (0.5 W) to 2 ms (2.2 W). Figure 4(c) shows the q dependence of $\langle\tau\rangle$. For 0 W normal diffusion is observed and $\langle\tau\rangle$ scales with q^{-2}. For increasing pump power a transition from normal to superdiffusion is observed and the scaling of $\langle\tau\rangle$ with q changes approaching a slope of approximately -1 at 2.2 W. In addition, Fig. 4(d) shows the dependence of the compressing exponent γ on q. Similar to what is observed for the Au$_{50}$ particles, γ decreases with increasing q and approaches 1.0 at high q. Apart from the high-q limit, the values of γ increase with increasing pump power at a given q. Again, we attribute these findings to a significant increase of the effective average temperature in the scattering volume due to photothermal heating and the flow induced by the convection roll. The influence of this photothermal heating on the swelling state of the hydrogel shell will be discussed in Sec. IV C.

We also performed pump-probe experiments with the Au$_{27}$-PMEO$_2$MA core-shell microgels. Figure 5(a) shows representative ICFs recorded at 0, 1.1, and 2.2 W. With increasing pump power, the ICFs decay faster. Similar to the case for the Au$_{35}$-PNIPAM microgels, the ICF at 0 W can be described by the cumulant fit (solid line), whereas it fails to describe the data for 1.1 and 2.2 W. In the latter cases, the ICFs can be described by Eq. (9) with compressing exponents $\gamma > 1.0$ (dashed lines). Figure 5(b) shows the q dependence of $\langle\tau\rangle$ recorded for different pump powers. Again, we observe normal diffusion for 0 W. With increasing pump power there is a transition from normal diffusion to superdiffusion. Figure 5(c) shows the dependence of the compressing exponent γ on q. For each pump power, γ decreases with increasing q and approaches 1.0 at high q. With increasing pump power we see an increase of γ at a given q. In brief, we find a similar behavior for the Au$_{27}$-PMEO$_2$MA and the Au$_{35}$-PNIPAM core-shell microgels. Independently of the chemical nature of the microgel shell, we find a transition from diffusive to superdiffusive behavior and compressing exponents γ larger than 1.0, which we attribute to the formation of convection rolls in response to the photothermal heating of the gold cores.

C. Photothermally induced shrinkage in the high-*q* limit

We now want to address the question whether the observed photothermal heating induces shrinkage of the thermoresponsive hydrogel shells. In the low- and mid-q range this is not easily possible due to the fact that the recorded ICFs are strongly compressed with compression exponents $\gamma > 1.0$ [see Figs. 4(d) and 5(c)] and the observed deviation from normal diffusion with the average relaxation time showing a weaker q dependence than q^{-2}. However, in the high-q limit, the compression exponent γ approaches values close to unity, also for higher pump powers. In this range the deviation from normal diffusion is less pronounced. Thus we use the relaxation times from the analysis of the measured ICFs in the high-q limit to determine the diffusion coefficient D_0 and assume that it corresponds to normal diffusion. In principle, one can now use the Stokes-Einstein equation (6) to calculate the hydrodynamic radius R_h of the core-shell microgels. However, one has to take into account (i) the temperature T in the scattering volume, (ii) the viscosity $\eta(T)$ of the dispersing medium at this temperature [see Eq. (7)], and (iii) that also R_h

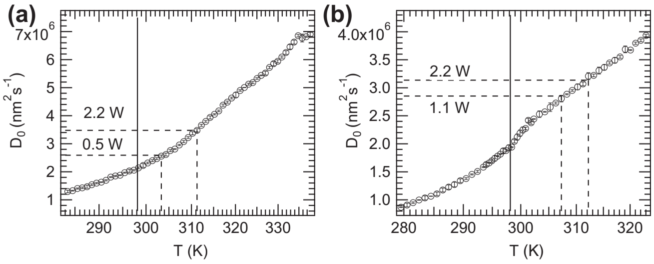

FIG. 6. Effective temperature-dependent diffusion coefficient $D(T)$ for (a) the Au$_{35}$-PNIPAM and (b) the Au$_{27}$-PMEO$_2$MA core-shell particles derived from the swelling curves in the Appendix. The vertical solid lines mark the reference temperature 25 °C (298.15 K) corresponding to a pump power of 0 W. The horizontal dashed lines correspond to the experimentally determined values of the diffusion coefficients determined in the high-q limit. The vertical dashed lines mark the temperatures at the intercepts with the $D(T)$ data points from swelling curves.

is a function of temperature for our thermoresponsive colloids. Since we can measure R_h as a function of temperature by standard temperature-dependent DLS (see Figs. 7 and 8 in the Appendix), we can calculate the diffusion coefficient $D(T)$ according to Eq. (6) for different temperatures. Figure 6 shows the respective results for the Au_{35}-PNIPAM [Fig. 6(a)] and the Au_{27}-$PMEO_2MA$ [Fig. 6(b)] core-shell microgels. Based on these plots and the diffusion coefficients determined at the high-q limit for both particles and different pump powers (horizontal dashed lines), the corresponding effective temperatures in the scattering volume (vertical dashed lines) can be estimated. The reference states at 25 °C (298.15 K) and 0 W pump power are indicated by solid vertical lines. For the Au_{35}-PNIPAM microgels, effective temperatures of approximately 30 °C (0.5 W pump power) and 38 °C (2.2 W) can be estimated. While the microgels will still be in a highly swollen state at 30 °C, a significant deswelling occurs at 38 °C. From a direct comparison with the swelling curve in the Appendix [Fig. 7(f)] we expect that a pump power of 2.2 W will induce a reduction of R_h from 115 nm (0 W, 25 °C) to approximately 100 nm. For the Au_{27}-$PMEO_2MA$ core-shell microgels we estimate the effective temperatures to reach approximately 34 °C (1.1 W pump power) and 39 °C (2.2 W). From a direct comparison with the swelling curve in the Appendix [Fig. 8(e)] we expect that a pump power of 2.2 W will induce a reduction of R_h from 127 nm (0 W, 25 °C) to approximately 110 nm. Thus, for both core-shell microgels a significant reduction in the shell thickness due to the photothermally induced volume phase transition of the thermoresponsive shells is observed.

V. CONCLUSION

We have measured the intensity-time autocorrelation functions of gold and hydrogel core-shell particles by angle-dependent dynamic light scattering using a two-beam pump-probe setup. While the pump laser was used to optically heat the plasmonic gold cores, only the scattered light from the probe laser was detected and used to generate the correlation functions. Under photothermal heating conditions, stretched exponential fits had to be used to satisfyingly describe the experimental correlation data. Stretching exponents $\gamma \geqslant 1$ were determined with values increasing with increasing pump power and decreasing momentum transfer q. At the highest accessible q the stretching exponents approached unity. Analysis of the angle-dependent data revealed a transition from normal diffusion with relaxation times that scale with q^{-2} for zero pump power to superdiffusion for increasing pump power. These effects were assigned to a pronounced increase in effective temperature in the scattering volume of the sample rather than a local heating effect in the close proximity of the absorbing gold nanoparticle cores. For a pump power of 2.2 W corresponding to an irradiance of $1.2 \times 10^4\ \mathrm{W\,cm^{-2}}$, an effective increase in temperature of approximately 10 K was estimated.

We demonstrated that the combination of plasmonic metal nanoparticles with thermoresponsive polymers in the form of colloids with a well-defined core-shell structure is suited for pronounced photothermal actuation, i.e., electromagnetic energy is converted to mechanical work. In this case the temperature increase induced by the photothermal actuation of the gold nanoparticle cores results in a significant shrinkage of the hydrogel shells. This shrinkage is the result of a significant change in the local temperature in the scattering volume that furthermore causes a transition from normal diffusion to superdiffusion. This transition in diffusion has mostly been ignored or not noticed in related works in the literature. Thus, with this work we demonstrate the importance of angle-dependent dynamic light scattering experiments, which can provide information on different length scales $L \propto \frac{1}{q}$, and careful analysis of the recorded intensity-time autocorrelation functions.

ACKNOWLEDGMENTS

M.K. acknowledges financial support from the Deutsche Forschungsgemeinschaft through the Emmy Noether program (Grant No. KA3880/1-1). The authors thank Tobias Honold and Joseph P. S. Fitzgerald for fruitful discussions. We would also like to thank Stephan Förster (Institue of Complex Systems, Forschungszentrum Jülich, Germany) for access to the dynamic light scattering setup.

APPENDIX: SUPPORTING INFORMATION

1. Materials

Gold(III) chloride hydrate (Aldrich, 99.9999%), L-ascorbic acid (Aldrich, >99%), cetyltrimethylammonium chloride (CTAC) (Aldrich, 25 wt. %, H_2O), N-isopropylacrylamide (Aldrich, 97%), N, N'-methylenbisacrylamide (Aldrich, 99%), potassium persulfate (Aldrich, 99%), aqueous KI/I_2 solution (Merck, 0.05M I_2, 25 $\mathrm{g\,l^{-1}}$ KI), hydrochloric acid (Bernd Kraft GmbH, 37%), and nitric acid (Merck, 65%) were used as received. 2-(2-methoxyethoxy)ethyl methacrylate (Sigma-Aldrich, 95%) was passed through a column of basic alumina to remove the inhibitor prior to use. National Institute of Standards and Technology traceable polystyrene particles (nominal diameter of 60 nm) were received from ThermoFisher Scientific. Water was purified using a Milli-Q system (Millipore). The resistivity of the water was 18.2 MΩ cm.

2. Synthesis of citrate-stabilized gold nanoparticles

Citrate-stabilized gold nanoparticles were synthesized according to a seeded-growth protocol by Bastús *et al.* [33]. Next, 100 ml of a 2.2 mM sodium citrate solution were heated until boiling. Then 667 μl of an aqueous 25 mM $HAuCl_4$ solution were added quickly under strong stirring. After the color changed from yellow to red, the dispersion was allowed to cool down to 90 °C.

The first batch of seeded-growth particles was synthesized by three subsequent additions of 667 μl of an aqueous 25 mM $HAuCl_4$ solution to the reaction mixture. Between each addition step, the reaction was allowed to proceed for 30 min. Then, 30 min after the last addition, 37 ml of the solution were withdrawn as a first batch of particles, Au_{15}, with the number in the subscript indicating the mean particle diameter from TEM. For the second batch of particles, seeded growth was continued by first adding 37 ml of a 2.2 mM solution of sodium citrate, previously heated to 90 °C, to the reaction medium and then by adding 667 μl of an aqueous 25 mM $HAuCl_4$ solution. The latter addition of the $HAuCl_4$ solution was subsequently repeated for another six times in the same manner as previously described for the first batch of particles. Finally, the dispersion was allowed to cool to room temperature, leading to the second batch of particles, Au_{50}.

3. Synthesis of Au-PNIPAM core-shell colloids

Au_{18}-PNIPAM core-shell microgels with 25 mol % nominal content of cross-linker [N,N'-methylenebisacrylamide (BIS)] were prepared by seeded precipitation polymerization as previously described [41]. We used a monomer concentration of 0.02 mol l^{-1}, initiator concentration of 0.15 μmol l^{-1}, and cross-linker concentration of 25 mol % with respect to the monomer concentration. After the polymerization, the particles were purified by repeated centrifugation and redispersion in Milli-Q water and then freeze-dried for further use.

The gold cores of the Au_{18}-PNIPAM microgels were then subsequently overgrown with gold in order to increase the absorption cross section of the cores at a wavelength of 532 nm. A previously published protocol was adopted [36]. First, a 1 wt. % aqueous stock solution of the Au_{18}-PNIPAM microgels was diluted with the same volume of 100 mM CTAC solution. Next, 500 μl of this stock solution were added to 10 ml of a CTAC solution (2.5 mM). Then 311 μl of a freshly prepared ascorbic acid solution (10 mM) were added under heavy stirring. Next, 4.8 ml of a solution containing 0.5 mM $HAuCl_4$ and 5 mM CTAC were added dropwise under heavy stirring. After 20 min two additional overgrowth steps were performed by adding 54 μl ascorbic acid solution (10 mM) and 800 μl of a solution containing 0.5 mM $HAuCl_4$ and 5 mM CTAC, respectively for each growing step. This overgrowth resulted in average core diameter of 35 nm and thus the microgels are referred to as Au_{35}-PNIPAM. Purification was performed by centrifugation at 3740 relative centrifugal force (rcf) for 30 min and redispersion in Milli-Q water. Centrifugation and redispersion were repeated three times. Afterward, the particles were dialyzed (Spectra/Por 4, molecular weight cutoff: 12–14 kD) against Milli-Q water for 72 h at room temperature and 24 h at 40 °C with exchange of water every 12 h in order to remove residual CTAC.

4. Synthesis of nonabsorbing PNIPAM microgels

Nonabsorbing PNIPAM reference microgels were prepared by dissolution of the gold core of Au_{18}-PNIPAM core-shell microgels using aqua regia. For this purpose, 3 ml of 37% hydrochloric acid were mixed with 1 ml of 65% nitric acid and after 20 min diluted with water by a factor of 5. Then 750 μl of the diluted aqua regia were added to 1200 μl of a 0.17 wt. % dispersion of Au_{18}-PNIPAM microgel particles under heavy stirring. After 4 h the particles were purified by centrifugation at 3740 rcf for 30 min. The supernatant was discarded and the precipitate redispersed in Milli-Q water. Centrifugation and redispersion were repeated three times.

5. Synthesis of Au-PMEO$_2$MA core-shell colloids

Au_{18}-PMEO$_2$MA with a nominal cross-linker density (BIS) of 15 mol % were prepared according to a procedure similar to that for the Au_{18}-PNIPAM particles. A monomer concentration of 0.02 mol l^{-1}, an initiator concentration of 0.15 μmol l^{-1}, and cross-linker concentration of 15 mol % with respect to the monomer concentration was used. The polymerization was conducted in 50 mL of Milli-Q water at 70 °C. After 3 h, the particles were purified by centrifugation at 11000 rcf for 45 min. The supernatant was discarded and the precipitate redispersed in 20 mL of Milli-Q water. Centrifugation and redispersion were repeated three times.

Overgrowth of Au_{18}-PMEO$_2$MA microgels was done as described before for the Au_{35}-PNIPAM microgels using a ratio of ascorbic acid to Au^{3+} of 26:1. This resulted in an average core diameter of 27 nm and thus the microgels are referred to as Au_{27}-PMEO$_2$MA. The microgels were purified by repeated centrifugation and redispersion in Milli-Q water as described before.

6. Characterization methods

UV-visible absorbance spectra were recorded with an Agilent 8453 spectrophotometer, covering a spectral range of 190–1100 nm. The sample temperature was adjusted by a circulating water bath (Julabo F30-C) and controlled by a PT100 sensor placed in a cuvette filled with silicon oil. Spectra from dilute dispersions were measured using quartz glass cells with 1 cm path length. All spectra were background corrected by measuring the respective solvent first. The concentration of Au^0 was determined from the absorption at $\lambda = 400$ nm according to Ref. [42]. Transmission electron microscopy images were recorded using a Zeiss/CEM902 TEM operating at an acceleration voltage of 80 kV. Transmission electron microscopy samples were prepared on carbon coated copper grids (200 mesh, Electron Microscopy Sciences) by drying droplets (10 μl) of dilute, aqueous particle dispersions.

7. Microgel characterization

Figures 7(a)–7(c) show TEM images of the PNIPAM microgels after core dissolution and the core-shell microgels Au_{18}-PNIPAM and Au_{35}-PNIPAM, respectively. The Au_{18}-PNIPAM [Fig. 7(b)] and the Au_{35}-PNIPAM microgels [Fig. 7(c)] have a well-defined core-shell morphology with single gold nanoparticle cores. These cores can be clearly distinguished from the hydrogel shells due to the pronounced difference in electron density between the cores and the PNIPAM shells. The absence of high-contrast nanoparticle cores in Fig. 7(a) manifests the success of the core dissolution for the PNIPAM reference microgels. Size histograms for the gold cores determined from TEM images are shown in Fig. 7(d). The mean radii of the gold cores of Au_{18}-PNIPAM and Au_{35}-PNIPAM are 8.6 and 18 nm, respectively. UV-vis absorbance spectra measured from dilute aqueous dispersions are shown in Fig. 7(e). For the PNIPAM microgels (gray) a continuous increase in absorbance with decreasing wavelength is observed. This is characteristic for the significant light scattering by the microgels in the visible wavelength range. In addition to the scattering contribution, the spectra of both core-shell

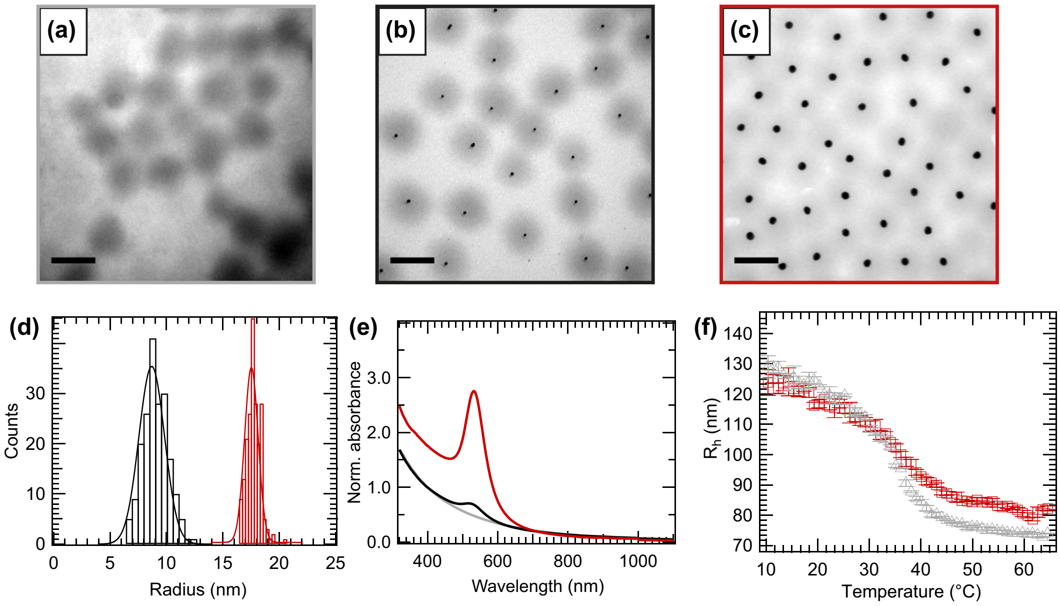

FIG. 7. TEM micrographs of (a) nonabsorbing PNIPAM microgels and (b) Au_{18}-PNIPAM and (c) Au_{35}-PNIPAM core-shell microgels. The scale bars correspond to 200 nm. (d) Size histograms of the gold cores obtained from TEM images of Au_{18}-PNIPAM (black) and Au_{35}-PNIPAM (red) particles. (e) UV-vis absorbance spectra of PNIPAM microgels (gray) and Au_{18}-PNIPAM (black) and Au_{35}-PNIPAM core-shell microgels (red) measured at 25 °C. (f) Hydrodynamic radius as a function of temperature for PNIPAM microgels (gray) and Au_{35}-PNIPAM core-shell microgels (red).

microgels feature LSP resonance peaks at approximately 530 nm. Due to the significantly larger absorption cross section of the larger cores of the Au_{35}-PNIPAM microgels, the corresponding spectrum shows a much more pronounced LSP resonance (red spectrum) as compared to the Au_{18}-PNIPAM microgels (black spectrum). Figure 7(f) shows swelling curves of the PNIPAM microgels and the Au_{35}-PNIPAM core-shell microgels measured by temperature-dependent DLS. Both samples show the typical volume phase transition behavior with a continuously decreasing hydrodynamic radius with increasing temperature in the vicinity of the volume phase transition temperature. Except for slight variations in size at higher temperatures, both swelling curves overlap nicely. For both samples a volume phase transition temperature of

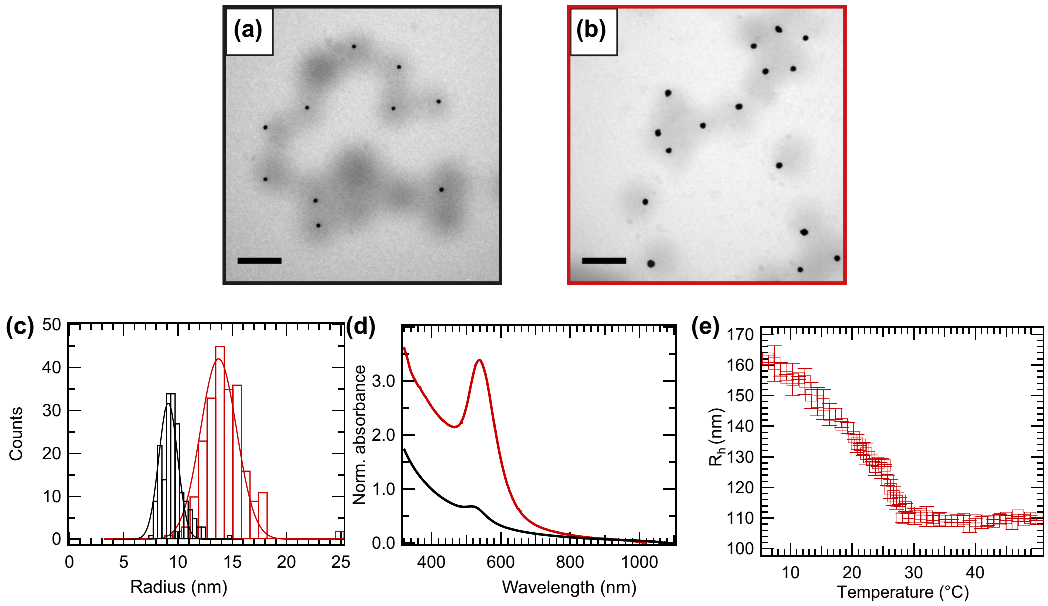

FIG. 8. TEM micrographs of (a) Au_{18}-PMEO$_2$MA and (b) Au_{27}-PMEO$_2$MA core-shell microgels. The scale bars correspond to 200 nm. (c) Size histograms of the gold cores obtained from TEM images of Au_{18}-PMEO$_2$MA (black) and Au_{27}-PMEO$_2$MA core-shell microgels (red). (d) UV-vis absorbance spectra of Au_{18}-PMEO$_2$MA (black) and Au_{27}-PMEO$_2$MA core-shell microgels (red) measured at 25 °C. (e) Hydrodynamic radius as a function of temperature for the Au_{27}-PMEO$_2$MA core-shell microgels.

approximately 35 °C can be determined. This value agrees well with measurements on core-shell microgels with similar degrees of cross-linking from the literature [34].

Figures 8(a) and 8(b) show TEM images of the Au_{18}-$PMEO_2MA$ and the Au_{27}-$PMEO_2MA$ core-shell microgels. Similar to the Au-PNIPAM microgels, the well-defined core-shell morphology with single gold nanoparticle cores well encapsulated by the hydrogel shells can be seen. The TEM size histograms of the gold cores in Fig. 8(c) provide mean radii of 9.2 and 13.7 nm for the Au_{18}-$PMEO_2MA$ and the Au_{27}-$PMEO_2MA$ core-shell microgels, respectively. Figure 8(d) shows UV-vis absorbance spectra measured from dilute aqueous dispersions. Both samples show the characteristic increase in absorbance with decreasing wavelength related to the scattering of the relatively large hydrogel shells. In addition, both core-shell microgels feature LSP resonance peaks at approximately 530 nm with the stronger resonance peak for the sample with the larger cores (Au_{27}-$PMEO_2MA$, red spectrum). Figure 8(e) shows a swelling curve of the Au_{27}-$PMEO_2MA$ core-shell microgels. The hydrodynamic radius measured by DLS decreases continuously with increasing temperature in the vicinity of the volume phase transition temperature of approximately 21 °C. This value is in agreement to reports in the literature [43].

8. Pump-probe dynamic light scattering measurements

An ALV/CGS-8F goniometer system with an ALV-5000 multiple tau digital correlator was used for all light scattering experiments in this work. The device was equipped with a HeNe laser (JDS Uniphase, $\lambda = 632.8$ nm, 21 mW) and a frequency-doubled Nd:YAG laser (Verdi Coherent, $\lambda = 532$ nm, 2.2 W). Both light sources can be operated simultaneously or on their own. Both beams were focused on the same scattering volume using a dichroic mirror and a biconvex lens with a focal length of 350 mm. The sample cuvettes were placed in a toluene bath in the rotation center of the goniometer. The temperature of the toluene bath was controlled using a circulating water bath (Haake F6). The PT100 sensor, located inside the toluene bath, was calibrated using an external thermometer [digital precision thermometer (VWR) accuracy ±0.05°]. The temperature was measured inside a cuvette, which was filled with silicon oil and placed in the toluene bath.

Samples were prepared by diluting freeze-dried samples or stock solutions, respectively. The samples were filtered using PTFE syringe filters with a pore size of 5 μm and filled into cylindrical quartz cells, which were cleaned with freshly distilled acetone.

Three ICFs were measured for each measurement condition, i.e., scattering angle and temperature. The measurement time for each run was between 60 and 180 s depending on the measured count rate. For angle-dependent measurements the scattering angle was varied in a range of 30°–150° in steps of 10°.

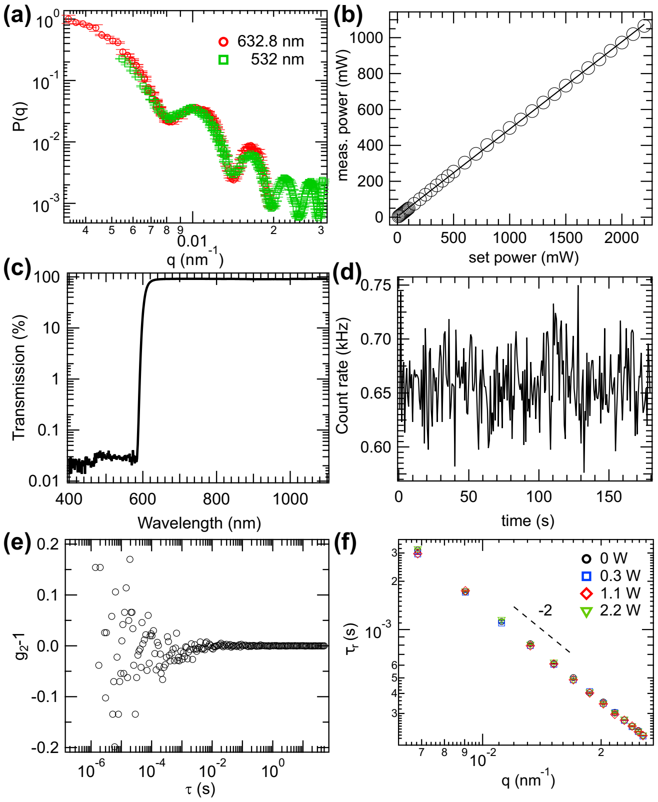

FIG. 9. (a) Static light scattering profiles of polystyrene particles with a diameter of 1 μm recorded with the HeNe ($\lambda = 632.8$ nm) and the Nd:YAG laser ($\lambda = 532$ nm). (b) Experimentally measured power of the Nd:YAG laser at the position of the beam stop as a function of the set power at the control unit of the laser. (c) Transmission of the longpass filter used as a function of the wavelength. (d) Count rate histogram for a PS standard at a scattering angle of 30° and only the Nd:YAG operating at 2.2 W with the longpass filter placed in front of the detection optics. (e) Corresponding intensity-time autocorrelation function from the measurement shown in (d). (f) The q dependence of τ_r for PS particles measured at pump powers of 0, 0.3, 1.1, and 2.2 W.

For temperature-dependent measurements, measurements were performed from 10° to 65° in steps of 1° at a scattering angle of 60°. If not stated otherwise, the ICFs were analyzed by using the method of cumulants [37]. The temperature-dependent refractive index and viscosity of water were calculated according to Refs. [32,44]. Prior to PP DLS measurements on absorbing colloids, we performed several reference measurements to ensure, e.g., the proper alignment of the instrument. Figure 9(a) shows the SLS profiles of nonabsorbing PS reference particles with a diameter of 1 μm recorded separately with both light sources. Due to the relatively large size of these particles, SLS resolves the form factor $P(q)$ of the particles with several pronounced oscillations. Most importantly, the SLS profiles measured with the two lasers perfectly overlap. This manifests the good alignment of both lasers on the same scattering volume. A slight variation in beam alignment would cause deviations in q and thus the form factors measured with both lasers would not be superimposed. Next we determined the expected power of the pump laser (Nd:YAG) at the sample position. A power meter (Coherent, FieldMAXII-TOP) was used to measure the power of the beam after passing the toluene bath without sample. The beam stop was removed and the power meter placed at the position of the beam stop. Figure 9(b) shows the measured laser power as a function of the set light power at the control unit of the laser. To estimate the corresponding irradiances at the scattering volume, we calculated the Gaussian beam diameter d_0 according to [45]

$$d_0 \approx \frac{2\lambda}{\pi \,\mathrm{NA}}, \tag{A1}$$

where λ is the wavelength of the light source (532 nm) and NA the numerical aperture given by [45]

$$\mathrm{NA} \approx n\frac{d_L}{2f}. \tag{A2}$$

Here n is the refractive index of air, d_L the beam diameter before the lens (2.25 mm), and f the focal length of the lens (350 mm). A beam diameter of $d_0 = 105\ \mu\mathrm{m}$ is obtained from this estimation. Taking into account the measured laser power and this beam diameter, irradiances I between 5.6×10^2 and $1.2 \times 10^4\ \mathrm{W\,cm^{-2}}$ are estimated for our experiments. In order to perform PP DLS experiments where only the scattered light from the probe laser is used to analyze the colloid diffusion, we placed a longpass filter with a cutoff at 600 nm in front of the detector. Figure 9(c) shows a transmission spectrum of the filter measured by UV-vis extinction spectroscopy. The filter has an optical density of 1.5 at 532 nm. To prove whether this filter blocks off scattered light from the pump laser efficiently, we performed measurements with only the pump laser operated at 2.2 W using the nonabsorbing PS particles as strongly scattering reference. Figure 9(d) shows the count rate histogram recorded at a scattering angle of 30°. The corresponding ICF is shown in Fig. 9(e). The absence of any correlation and the very low count rate in Fig. 9(d) reveal that the scattered light from the pump laser is efficiently blocked by the longpass filter.

In order to analyze the potential influence of photon pressure from the pump laser we performed PP DLS experiments at various pump powers using the nonabsorbing PS reference particles. We recorded ICFs from the scattered light of the probe laser over a broad angular range for each pump power. Independently of the pump power, the measured ICFs $g_2(\mathbf{q}, \mathbf{t})$ could be analyzed by the method of cumulants providing the relaxation times [Eq. (8)]. Figure 9(f) shows the relaxation times τ_r as a function of q measured at pump powers between 0 and 2.2 W in double logarithmic representation. For all pump powers a linear relation with nearly the same slope close to −2 is observed. This indicates that normal diffusion occurs.

9. Absorption cross section

The temperature profiles around Au_{15} and Au_{50} nanoparticles were calculated based on the absorption cross section calculated using Mie theory [46] and the MiePlot software [47]. For the particle radius, the TEM diameter was used. The refractive index of gold was taken from Johnson and Christy [48]. The refractive index of water (1.33) was assumed for the surrounding media.

---

[1] C. Bohren and D. Huffman, *Absorption and Scattering of Light by Small Particles* (Wiley, New York, 1983).

[2] U. Kreibig and M. Vollmer, *Optical Properties of Metal Clusters* (Springer, Berlin, 1995).

[3] J. Rodríguez-Fernández, J. Pérez-Juste, F. J. G. de Abajo, and L. M. Liz-Marzán, Langmuir **22**, 7007 (2006).

[4] P. Mulvaney, Langmuir **12**, 788 (1996).

[5] M. B. Müller, C. Kuttner, T. A. F. König, V. V. Tsukruk, S. Förster, M. Karg, and A. Fery, ACS Nano **8**, 9410 (2014).

[6] L. M. Liz-Marzán, Langmuir **22**, 32 (2006).

[7] C. Sönnichsen, T. Franzl, T. Wilk, G. von Plessen, J. Feldmann, O. Wilson, and P. Mulvaney, Phys. Rev. Lett. **88**, 077402 (2002).

[8] S. Berciaud, L. Cognet, G. A. Blab, and B. Lounis, Phys. Rev. Lett. **93**, 257402 (2004).

[9] G. Baffou and R. Quidant, Laser Photon. Rev. **7**, 171 (2013).

[10] G. Baffou, R. Quidant, and F. J. G. de Abajo, ACS Nano **4**, 709 (2010).

[11] P. M. Paulo, A. Gaiduk, F. Kulzer, S. G. Krens, H. P. Spaink, T. Schmidt, and M. Orrit, J. Phys. Chem. C **113**, 11451 (2009).

[12] D. Rings, R. Schachoff, M. Selmke, F. Cichos, and K. Kroy, Phys. Rev. Lett. **105**, 090604 (2010).

[13] R. Raduenz, D. Rings, K. Kroy, and F. Cichos, J. Phys. Chem. A **113**, 1674 (2009).

[14] G. Zhang, C. Hsu, C. Lan, R. Gao, Y. Wen, and J. Zhou, ACS Appl. Mater. Interfaces **11**, 2254 (2019).

[15] S. Cormier, T. Ding, V. Turek, and J. J. Baumberg, Adv. Opt. Mater. **6**, 1701281 (2018).

[16] I. Gorelikov, L. M. Field, and E. Kumacheva, J. Am. Chem. Soc. **126**, 15938 (2004).

[17] H. Schild, Prog. Polym. Sci. **17**, 163 (1992).

[18] K. Yanase, R. Buchner, and T. Sato, Phys. Rev. Mater. **2**, 085601 (2018).

[19] M. Karg, A. Pich, T. Hellweg, T. Hoare, L. A. Lyon, J. J. Crassous, D. Suzuki, R. A. Gumerov, S. Schneider, I. I. Potemkin *et al.*, Langmuir **35**, 6231 (2019).

[20] M. Karg, Colloid Polym. Sci. **290**, 673 (2012).

[21] M. Karg and T. Hellweg, Curr. Opin. Colloid Interface Sci. **14**, 438 (2009).

[22] M. Das, N. Sanson, D. Fava, and E. Kumacheva, Langmuir **23**, 196 (2007).

[23] M. Lehmann, W. Tabaka, T. Möller, A. Oppermann, D. Wöll, D. Volodkin, S. Wellert, and R. von Klitzing, Langmuir **34**, 3597 (2018).

[24] S. Hormeño, N. G. Bastús, A. Pietsch, H. Weller, J. R. Arias-Gonzalez, and B. H. Juárez, Nano Lett. **11**, 4742 (2011).

[25] S. Hormeño, P. Gregorio-Godoy, J. Pérez-Juste, L. M. Liz-Marzán, B. H. Juárez, and J. R. Arias-Gonzalez, Small **10**, 376 (2013).

[26] J. Rodríguez-Fernández, M. Fedoruk, C. Hrelescu, A. A. Lutich, and J. Feldmann, Nanotechnology **22**, 245708 (2011).

[27] S. Murphy, S. Jaber, C. Ritchie, M. Karg, and P. Mulvaney, Langmuir **32**, 12497 (2016).

[28] W. Schaertl and C. Roos, Phys. Rev. E **60**, 2020 (1999).

[29] M. Schwägler, C. Nowak, J. Hoffmann, and W. Schärtl, J. Phys. Chem. C **113**, 15124 (2009).

[30] A. Sehgal and T. A. Seery, Macromolecules **32**, 7807 (1999).

[31] P. Pusey, in *Neutrons, X-rays and Light: Scattering Methods Applied to Soft Condensed Matter*, edited by T. Zemb and P. Lindner (Elsevier Science, Amsterdam, 2002), Chap. 4, pp. 203–220.

[32] C. H. Cho, J. Urquidi, S. Singh, and G. W. Robinson, J. Phys. Chem. B **103**, 1991 (1999).

[33] N. G. Bastús, J. Comenge, and V. Puntes, Langmuir **27**, 11098 (2011).

[34] M. Karg, S. Jaber, T. Hellweg, and P. Mulvaney, Langmuir **27**, 820 (2011).

[35] J. Turkevich, P. C. Stevenson, and J. Hillier, Discuss. Faraday Soc. **11**, 55 (1951).

[36] T. Honold, K. Volk, A. Rauh, J. P. S. Fitzgerald, and M. Karg, J. Mater. Chem. C **3**, 11449 (2015).

[37] B. J. Frisken, Appl. Opt. **40**, 4087 (2001).

[38] A. Madsen, R. L. Leheny, H. Guo, M. Sprung, and O. Czakkel, New J. Phys. **12**, 055001 (2010).

[39] C. P. Lindsey and G. D. Patterson, J. Chem. Phys. **73**, 3348 (1980).

[40] O. D. Parashchuk, T. V. Laptinskaya, M. S. Ananieva, and D. Y. Paraschuk, Soft Matter **7**, 5585 (2011).

[41] A. Rauh, T. Honold, and M. Karg, Colloid Polym. Sci. **294**, 37 (2015).

[42] T. Hendel, M. Wuithschick, F. Kettemann, A. Birnbaum, K. Rademann, and J. Polte, Anal. Chem. **86**, 11115 (2014).

[43] A. Lapresta-Fernández, J. M. García-García, R. París, R. Huertas-Roa, A. Salinas-Castillo, S. A. de la Llana, J. F. Huertas-Pérez, N. Guarrotxena, L. F. Capitán-Vallvey, and I. Quijada-Garrido, Part. Part. Syst. Charact. **31**, 1183 (2014).

[44] A. H. Harvey, J. S. Gallagher, and J. M. H. L. Sengers, J. Phys. Chem. Ref. Data **27**, 761 (1998).

[45] D. Meschede, *Optik, Licht und Laser* (Vieweg Teubner, Leipzig, 2005).

[46] G. Mie, Ann. Phys. (Leipzig) **330**, 377 (1908).

[47] http://www.philiplaven.com/mieplot.htm.

[48] P. B. Johnson and R. W. Christy, Phys. Rev. B **6**, 4370 (1972).